

Rational design and optimization of plasmonic nanoarrays for surface enhanced infrared spectroscopy

Vladimir Liberman,^{1,*} Ronen Adato,^{2,4} Thomas H. Jeys,¹ Brian G. Saar,¹
Shyamsunder Erramilli,^{3,4,5} and Hatice Altug^{2,3,4}

¹Lincoln Laboratory, Massachusetts Institute of Technology, Lexington, Massachusetts 02420, USA

²Department of Electrical and Computer Engineering, Boston University, Boston, Massachusetts 02215, USA

³Division of Materials Science and Engineering, Boston University Boston, Massachusetts 02215, USA

⁴Boston University Photonics Center, Boston, Massachusetts 02215, USA

⁵Department of Physics & Biomedical Engineering, Boston University Boston, Massachusetts 02215, USA

*vlad@ll.mit.edu

Abstract: We present an approach for rational design and optimization of plasmonic arrays for ultrasensitive surface enhanced infrared absorption (SEIRA) spectroscopy of specific protein analytes. Motivated by our previous work that demonstrated sub-attomole detection of surface-bound silk fibroin [Proc. Natl. Acad. Sci. U.S.A. **106**, 19227 (2009)], we introduce here a general framework that allows for the numerical optimization of metamaterial sensor designs in order to maximize the absorbance signal. A critical feature of our method is the explicit compensation for the perturbative effects of the analyte's refractive index which alters the resonance frequency and line-shape of the metamaterial response, thereby leading to spectral distortion in SEIRA signatures. As an example, we leverage our method to optimize the geometry of periodic arrays of plasmonic nanoparticles on both Si and CaF₂ substrates. The optimal geometries result in a three-order of magnitude absorbance enhancement compared to an unstructured Au layer, with the CaF₂ substrate offering an additional factor of three enhancement in absorbance over a traditional Si substrate. The latter improvement arises from increase of near-field intensity over the Au nanobar surface for the lower index substrate. Finally, we perform sensitivity analysis for our optimized arrays to predict the effects of fabrication imperfections. We find that <20% deviation from the optimized absorbance response is readily achievable over large areas with modern nanofabrication techniques.

©2012 Optical Society of America

OCIS codes: (240.6680) Surface plasmons; (260.3910) Metal optics; (250.5403) Plasmonics; (300.6340) Spectroscopy, infrared.

References

1. R. Adato, A. A. Yanik, J. J. Amsden, D. L. Kaplan, F. G. Omenetto, M. K. Hong, S. Erramilli, and H. Altug, "Ultra-sensitive vibrational spectroscopy of protein monolayers with plasmonic nanoantenna arrays," Proc. Natl. Acad. Sci. U.S.A. **106**(46), 19227–19232 (2009).
2. C. Wu, A. B. Khanikaev, R. Adato, N. Arju, A. A. Yanik, H. Altug, and G. Shvets, "Fano-resonant asymmetric metamaterials for ultrasensitive spectroscopy and identification of molecular monolayers," Nat. Mater. **11**(1), 69–75 (2011).
3. V. Silin and A. Plant, "Biotechnological applications of surface plasmon resonance," Trends Biotechnol. **15**(9), 353–359 (1997).
4. J. N. Anker, W. P. Hall, O. Lyandres, N. C. Shah, J. Zhao, and R. P. Van Duyne, "Biosensing with plasmonic nanosensors," Nat. Mater. **7**(6), 442–453 (2008).
5. S. Wang, E. S. Forzani, and N. Tao, "Detection of heavy metal ions in water by high-resolution surface plasmon resonance spectroscopy combined with anodic stripping voltammetry," Anal. Chem. **79**(12), 4427–4432 (2007).

6. S. Wang, S. Ota, B. Guo, J. Ryu, C. Rhodes, Y. Xiong, S. Kalim, L. Zeng, Y. Chen, M. A. Teitell, and X. Zhang, "Subcellular resolution mapping of endogenous cytokine secretion by nano-plasmonic-resonator sensor array," *Nano Lett.* **11**(8), 3431–3434 (2011).
7. M. P. Jonsson, A. B. Dahlin, L. Feuz, S. Petronis, and F. Höök, "Locally functionalized short-range ordered nanoplasmonic pores for bioanalytical sensing," *Anal. Chem.* **82**(5), 2087–2094 (2010).
8. A. J. Haes, L. Chang, W. L. Klein, and R. P. Van Duyne, "Detection of a biomarker for Alzheimer's disease from synthetic and clinical samples using a nanoscale optical biosensor," *J. Am. Chem. Soc.* **127**(7), 2264–2271 (2005).
9. F. Neubrech, A. Pucci, T. W. Cornelius, S. Karim, A. García-Etxarri, and J. Aizpurua, "Resonant plasmonic and vibrational coupling in a tailored nanoantenna for infrared detection," *Phys. Rev. Lett.* **101**(15), 157403 (2008).
10. E. Cubukcu, S. Zhang, Y.-S. Park, G. Bartal, and X. Zhang, "Split ring resonator sensors for infrared detection of single molecular monolayers," *Appl. Phys. Lett.* **95**(4), 043113 (2009).
11. R. Bukasov and J. S. Shumaker-Parry, "Highly tunable infrared extinction properties of gold nanocrescents," *Nano Lett.* **7**(5), 1113–1118 (2007).
12. R. Adato, A. A. Yanik, C.-H. Wu, G. Shvets, and H. Altug, "Radiative engineering of plasmon lifetimes in embedded nanoantenna arrays," *Opt. Express* **18**(5), 4526–4537 (2010).
13. M. Osawa, "Surface-enhanced infrared absorption," in *Near-Field Optics and Surface Plasmon Polaritons*, S. Kawata, ed. (Springer Berlin / Heidelberg, 2001), pp. 163–187.
14. V. Liberman, R. Adato, A. Mertiri, A. A. Yanik, K. Chen, T. H. Jeys, S. Erramilli, and H. Altug, "Angle- and polarization-dependent collective excitation of plasmonic nanoarrays for surface enhanced infrared spectroscopy," *Opt. Express* **19**(12), 11202–11212 (2011).
15. S.-Y. Lin, T.-K. Wu, H.-J. Chiou, T. H.-S. Hsu, and C.-C. Lin, "Infrared microspectroscopic imaging as a probing tool to fast distinguish chemical compositions in calcified deposits of prostatic calculi and calcific tendonitis," *Spectroscopy* **25**(5), 207–216 (2011).
16. J. Anastassopoulou, E. Boukaki, C. Conti, P. Ferraris, E. Giorgini, C. Rubini, S. Sabbatini, T. Theophanides, and G. Tosi, "Microimaging FT-IR spectroscopy on pathological breast tissues," *Vib. Spectrosc.* **51**(2), 270–275 (2009).
17. M. Boulet-Audet, T. Buffeteau, S. Boudreault, N. Daugey, and M. Pézolet, "Quantitative determination of band distortions in diamond attenuated total reflectance infrared spectra," *J. Phys. Chem. B* **114**(24), 8255–8261 (2010).
18. B. D. Lawrence, F. Omenetto, K. Chui, and D. L. Kaplan, "Processing methods to control silk fibroin film biomaterial features," *J. Mater. Sci.* **43**(21), 6967–6985 (2008).
19. H. Arnolds, "Vibrational dynamics of adsorbates - Quo vadis?" *Prog. Surf. Sci.* **86**(1-2), 1–40 (2011).
20. R. F. Aroca, D. J. Ross, and C. Domingo, "Surface-enhanced infrared spectroscopy," *Appl. Spectrosc.* **58**(11), 324–338 (2004).
21. R. Forker, M. Gruenewald, and T. Fritz, "Optical differential reflectance spectroscopy on thin molecular films," *Annu. Rep. Sect. C Phys. Chem.*, March 9, (2012).
22. R. Qiang, R. L. Chen, and J. Chen, "Modeling Electrical Properties of Gold Films at Infrared Frequency Using FDTD Method," *Int. J. Infrared Millim. Waves* **25**(8), 1263–1270 (2004).
23. Film Wizard, Scientific Computing International.
24. E. D. Palik, *Handbook of Optical Constants of Solids* (Academic Press, 1998).
25. F. Bensebaa, P. L'Ecuyer, K. Faid, C. Py, T. J. Tague, and R. S. Jackson, "Grazing angle infrared microspectroscopy of micropatterned self-assembled monolayers," *Appl. Surf. Sci.* **243**(1-4), 238–244 (2005).
26. FDTD Solutions, Lumerical, Inc.
27. S. Kessentini, D. Barchiesi, T. Grosgees, and M. L. de la Chapelle, "Particle swarm optimization and evolutionary methods for plasmonic biomedical applications," in *2011 IEEE Congress on Evolutionary Computation (CEC)* (IEEE, 2011), 2315–2320.
28. J. Snyman, *Introduction to Basic Optimization Theory and Classical and New Gradient-Based Algorithms* (Springer Publishing, 2005).
29. T. T. Allen, *Introduction to Engineering Statistics and Six Sigma* (Springer Verlag, London, 2006).
30. D. Staiculescu, N. Bushyager, A. Obatoyinbo, L. J. Martin, and M. M. Tentzeris, "Design and optimization of 3-D compact stripline and microstrip Bluetooth/WLAN balun architectures using the design of experiments technique," *IEEE Trans. Antenn. Propag.* **53**(5), 1805–1812 (2005).
31. ECHIP, Velocity Pointe, LLC.

Introduction

Plasmonic metamaterial sensors have been a subject of increasing interest in recent years because they offer the capability to precisely engineer the interaction between electromagnetic radiation and analytes to perform highly sensitive measurements of absorption or refractive index changes [1–3]. Metamaterial sensors have shown a high degree of promise for ultrasensitive detection of chemicals and biomolecules in compact, low-power devices [4], and may find use in environmental sensing [5], biochemical assays [6, 7] and pathology [8], among other fields. The required plasmonic metamaterials have been developed at a wide

range of electromagnetic frequencies, from visible light to THz and beyond. Their use in the infrared region of the spectrum, however, is particularly attractive since essentially all molecules have intrinsic absorption features in the infrared that arise from their internal vibrational modes, allowing for chemically-specific sensing [1].

Design of plasmonic elements for mid-IR spectroscopy typically follows RF antenna analogues such as long rod-shaped particles [1, 9] or ring-resonators [10, 11] which provide the basic requisites of readily tunable resonance frequencies and high near-field enhancement. Additionally, since radiation damping dominates over intrinsic material absorbance in the mid-IR, designs that limit the damping lead to higher field enhancement and, thus, improved detection sensitivity [1, 12]. This consideration has been implemented both by leveraging diffractive coupling effects in periodic nanoparticle arrays [1] and, recently, by accessing the dark quadrupolar modes in a hybridized nanoparticle system [2].

While experimental demonstrations of the above principles may vary one or a few design parameters to illustrate a general trend, full optimization of device geometry is typically too costly or time consuming. In this work, we propose a systematic attack on this important problem of rational design of metamaterials. In contrast to previous methods which optimize on indirect proxies, such as resonance far-field quality factor or numerical non-observables, such as near-field enhancement, our approach optimizes absorbance, the observable quantity of interest. Benefits of absorbance optimization include: i) appropriate interaction of the electric field with the analyte's molecular dipole, ii) spatial averaging over localized hot spots, and iii) predicting spectra that can be directly compared with experimental data.

An important aspect of our method addresses the fact that, even for a properly tuned array, spectral interpretation of the resulting signals is not straightforward. Strong signal enhancement can lead to spectral distortion, or produce derivative-like spectra, often observed with SEIRA technique [13]. Spectral distortion arises from the refractive index variation in the vicinity of a strong absorption feature, as dictated by the Kramers-Kronig relation. This index variation causes local detuning of a plasmonic structure, whose resonance position is sensitive to the dielectric constant of the environment and the thickness of the dielectric overlayer. In fact, a recent paper has explored this additional index sensitivity to derive more information about the thickness of the adsorbates from the “distorted” reflectance signatures [2].

As a test platform for demonstrating our approach, we consider a two-dimensional tiled array of gold nanobar antennas that are individually tuned to plasmonically enhance the absorption peak of interest and, then, diffractively-coupled for additional signal enhancement [1, 12, 14]. This design achieves monolayer sensitivity at normal-incidence irradiation geometry, which is particularly well-suited for diffraction-limited infrared microscopy with potential applications in pathology [15, 16]. We demonstrate robust optimization methods for arriving at the array geometry for the highest expected absorbance for any spectral region of interest, and for various substrate refractive indices. We also discuss strategies for minimizing expected spectral distortion of absorbance that could interfere both with the array design and with subsequent measurement of adsorbates on the array. Finally, we discuss robustness of the final design with respect to deviation from the optimized dimensions. The approach taken can readily be applied to any arbitrary plasmonic geometry providing a straightforward technique to aid in the development and significantly improve the utility of plasmonic SEIRA sensors with undistorted chemical signatures.

Optimization framework

Bare Au layers

To provide a reference for our process of spectral optimization, we start with an unstructured Au layer covered with a thin film of the protein silk fibroin. The optical constants of silk fibroin have been measured previously, utilizing Attenuated Total Reflectance (ATR)

spectroscopy (Fig. 1) [17]. Less than 5% anisotropy was detected in the previous study; thus, for the purpose of this work we assume the optical constants of Fig. 1 to be fully isotropic. From an experimental point of view, silk fibroin is conveniently spun-cast onto a substrate with well-controlled thickness ranging from a single monolayer to microns [1, 18]. From a modeling point of view, the above optical constant data set with its doublet peaks at 6 μm - and 6.6 μm -wavelengths allows illustration of the array design for selective enhancement of different spectral region:

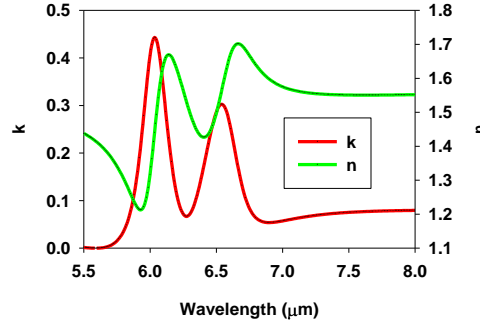


Fig. 1. Real and imaginary parts of refractive index of silk fibroin as measured in a previous work [17].

The underlying mechanisms of infrared absorption at metal surfaces have been recently reviewed [13, 19, 20]. In general, the probability for absorption is proportional to the square of the dipole moment matrix element along the direction of light polarization. For molecules in solid state or adsorbed on metal surfaces, the spatial orientation is fixed. Furthermore, it can be shown that for small perturbations of the dipole moment in its ground electronic state, the intensity of the infrared absorption is proportional to the incident electric field intensity $|E|^2$ and the change of dipole moment μ with vibrational coordinate Q as

$$A \propto \left| \frac{\partial \mu}{\partial Q} \right|_0^2 |E|^2 \quad (1)$$

In the above, the derivative is evaluated at equilibrium with respect to the vibrational coordinate. We define an effective absorbance for a flat Au film analogously to Differential Reflectance Spectroscopy [21] as

$$A_{Au} = \log \left(\frac{R_{bare,Au}}{R_{cov,Au}} \right) \quad (2)$$

In the above $R_{bare,Au}$ is the reflectance of a bare Au film, sufficiently thicker than the skin depth, which is ≈ 25 nm in the mid IR [22], and $R_{cov,Au}$ is the reflectance of the Au film covered with an adsorbed layer whose optical constants are given in Fig. 1.

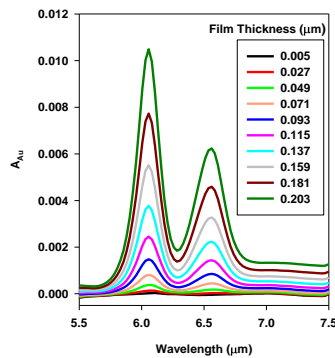


Fig. 2. Simulated absorbance response from a fibroin film for a range of thicknesses from 5 to 200 nm on an unstructured Au film.

Calculated absorbance signatures of the fibroin-covered bare Au film for normal incidence are shown in Fig. 2. These results are based on explicit solutions of Fresnel equations, utilizing a commercial thin film multilayer software package [23]. The optical constants of Au from the literature are used [24]. Since the state-of-the-art FTIR sensitivity for absorbance measurements is near 10^{-5} , the absorbances for the films below $0.05\mu\text{m}$ in thickness in Fig. 2 would be barely detectable without enhancement. In principle, a grazing incidence reflectance accessory can significantly enhance these weak signals [25], though mid IR grazing incidence objectives are expensive and cumbersome. Alternatively, nanoplasmonic arrays can enhance the normal incidence reflectance signal without introducing new optics or sacrificing lateral resolution for potential imaging applications.

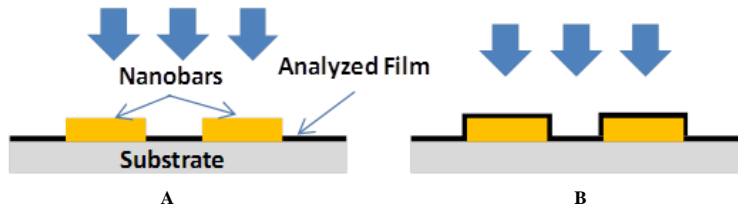


Fig. 3. Coverage geometry for a film on a substrate defining planar (A) and conformal (B) cases. Incident light direction is shown by large solid arrows.

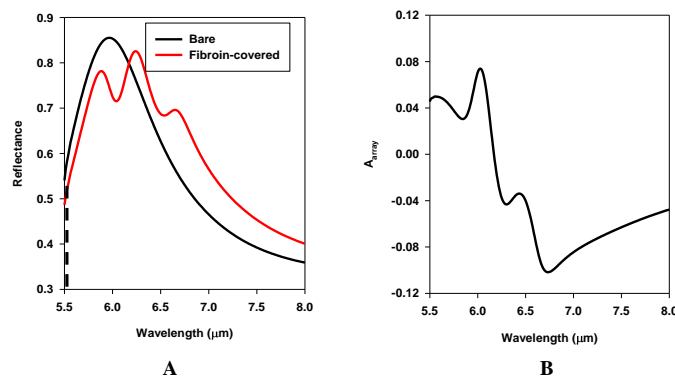


Fig. 4. Simulated absorbance response of a reference nanoplasmonic array covered with a 100-nm thick planar fibroin layer. A) Reflectance of a bare and fibroin-covered surface. The dashed vertical line (near $5.5\mu\text{m}$) indicates the position of the (1,0) diffracted edge (see Eq. (7)). B) Absorbance response from Eq. (3).

Development of the figure-of-merit for nanobar arrays

As we have previously shown [1], the absorbance signal strength from an unstructured Au layer can be improved orders of magnitude through the use of the diffractively coupled plasmonic nanoarray. By analogy with Eq. (2), we define an effective absorbance for a plasmonic nanoarray metamaterial as

$$A_{array} = \log \left(\frac{R_{bare}}{R_{cov}} \right) \quad (3)$$

In the above, R_{bare} and R_{cov} refer to the far-field reflectance for a bare and an analyte-covered array, respectively. For all the work here, incident light is assumed to be polarized along the long axis of the nanobar antennae in order to observe the plasmonic resonances. Light polarized along the short axis will not interact resonantly with the nanobars and will be mostly transmitted.

In this work we focus on the range of film thicknesses from 5 to 200 nm. The optical response from much thicker films is dominated by bulk effects and such films can be analyzed by conventional spectroscopic techniques, not requiring surface enhancement. For the thinnest films, we will distinguish between two regimes of coating geometries: “planar” and “conformal”, as shown in Fig. 3. In the earlier part of this study, we consider planar films. In the latter part of the paper, we address the impact of coverage geometry on array optimization (see Table 1 below).

We first consider an array geometry that was previously optimized experimentally based on its bare reflectance signature response [1] and studied computationally for a response at various angles of incidence [14]. The geometry consists of Au nanobar arrays on a Si substrate arranged in a square periodic lattice. The array length, width and thickness are 0.95 μm , 0.25 μm and 0.07 μm , respectively, and the periodicity in both dimensions is 1.6 μm . In Fig. 4, we plot the reflectance of such bare array and that of a corresponding array covered with a 100-nm thick planar fibroin film. This array reflectance is computed utilizing a commercial package [26], FDTD Solutions (Lumerical Corporation, Vancouver, Canada) and the computational procedure has been described in detail previously [14]. The 100-nm fibroin film thickness is chosen to fully submerge the 70-nm thick Au nanobars.

While we do see reflectance dips in Fig. 4(A), corresponding to the fibroin absorbance near 6- μm and 6.55- μm wavelengths, the peak array reflectance is red-shifted from the bare reference so that the absorbance signature, as defined by Eq. (3) is severely distorted (Fig. 4(B)). In fact, it would be difficult to match this spectrum to the original absorbance of Fig. 1 without post-processing. The spectral distortion, which is caused by the array sensitivity to the real part of the refractive index of the fibroin overlayer, makes it difficult to guide an optimization algorithm towards a design, enhanced for the chemically-specific *absorptive* contribution of the optical constants. A strategy for experimental corrections of such distortions upon spectral acquisition is needed so as to obtain a result that is easily interpretable based on familiar infrared spectral fingerprints.

Our approach to reducing the distortion of the spectrum is to utilize a more appropriate reference in Eq. (3) instead of the *bare* array reflectance. We replace R_{bare} with R_{ref} , a reflectance from a surface covered with a reference material, whose real part of the refractive index approximates that of the analyte, but whose absorption is zero. We define modified referenced absorbance, A_{ref} , as

$$A_{ref} = \log \left(\frac{R_{ref}}{R_{cov}} \right) \quad (4)$$

The simplest choice for the reference material that still retains consistency with Kramers-Kronig relations is the one with a constant n that is close to an average refractive index value of fibroin in the spectral region of interest. The choice of such value becomes clear after

computing A_{ref} for several refractive index values of the reference material, as shown in Fig. 5. The resonance wavelength of the nanoplasmonic array causes selective absorbance enhancement of the Amide I spectral region near 6.0 μm . We look for the absorption trace that has the flattest baseline surrounding just the 6- μm peak. The respective baseline for each trace is shown in Fig. 5 as a dashed line in the vicinity of the 6.0- μm absorbance peak. The flattest baseline is observed for the refractive index $1.4 < n < 1.5$ which corresponds to the value of the fibroin refractive index near the 6- μm absorption feature from Fig. 1.

Adopting A_{ref} absorbance definition from Eq. (4), we now need to choose a proper scalar figure of merit (FOM) for the optimization algorithm to design an array with optimum enhancement of an absorptive feature of interest. We propose the following procedure for computing a robust FOM:

1. For a given set of geometric parameters and a given overlayer thickness, compute R_{cov} , R_{ref} and A_{ref} from Eq. (4).
2. Apply linear baseline correction to A_{ref} over the wavelength range of interest. This correction is necessary to guide the optimizer towards absorption peak enhancement rather than a featureless reflectance offset.
3. Define FOM as baseline-corrected A_{ref} , averaged over the spectral range of interest. For example, to enhance the Amide I Fibroin feature of Fig. 1, spectral region from 5.75 to 6.25 μm is chosen.

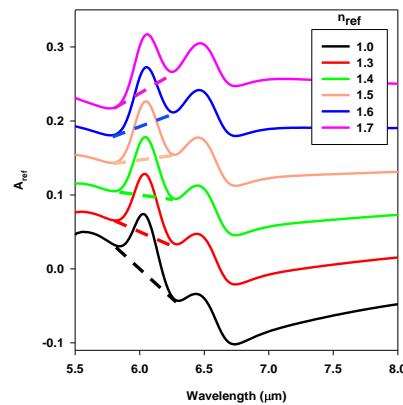


Fig. 5. Computed A_{ref} from Eq. (4) for several values of the reference refractive index. Dashed lines for each trace in the vicinity of the 6.0- μm peaks highlight position of the baseline.

The optimizations are performed by combining global Swarm Optimization (SO) method [27] with additional local parameter refinement that utilizes a steepest descent algorithm [28]. Both these methods are incorporated into the Lumerical software package [24]. To improve efficiency of the simulations, we start with SO method utilizing coarser meshing of the simulation domain and, once the optimum parameter space is identified, follow up with the finer mesh and the steepest descent algorithm. Optimization is performed for nanobar width, length, and period (both a square and a rectangular lattice have been considered).

The SO method requires a range of parameters for swarm exploration. In order to better guide the algorithm, we ensure that the selected range includes the estimated conditions for maximum field intensity enhancement over the spectral range of interest, based on the intuitive length scaling of the plasmonic resonance and the optimal periodicities associated with diffractive coupling effects [1,12]. The resonance wavelength for the individual antennae obeys the relation

$$\lambda_{res} = \frac{2}{m} n_{eff} L + C \quad (5)$$

where m is the order of the resonance mode, n_{eff} is the effective refractive index of the environment, L is the nanobar length and C is the fitting parameter related to a finite cross-section of the nanorods [12]. For $m = 1$ mode, the length of the nanobar is given by

$$L = \frac{\lambda_{res} - C}{2n_{eff}} \quad (6)$$

Previously, n_{eff} was found to be 2.7 for arrays on Si substrate and C is 0.16 μm for the 1st order resonance. Because the maximum field intensity enhancement occurs near the resonant wavelength, we allow the simulation to explore a $\pm 15\%$ range of lengths surrounding the value of L that would result in λ_{res} of 6 μm .

Furthermore, the array periodicity plays a role in increasing near-field enhancement by controlling the radiative damping of the plasmon resonance. In particular, the damping is substantially reduced at wavelengths slightly longer than the grating transition wavelength, i.e., the wavelength at which a given grating order transitions from evanescent to radiative in character. The critical period, d_c , which places this transition near the spectral region of interest, for the (1,0) order is found from

$$d_c = \frac{\lambda_{res}}{n_{sub}} \quad (7)$$

where n_{sub} is the refractive index of the substrate. A $\pm 15\%$ range of lengths for surrounding d_c was chosen for the SO parameter exploration.

Array width can also affect the position of the resonance, through the change in the effective nanobar cross-section [12]. Based on the range of widths explored in our fabrication work, we allowed the width to vary from 100 to 250 nm in the optimizations. As we will show in the sensitivity analysis section, the optimized FOM is only weakly dependent on the width.

Optimization results

Silicon substrate

For the first example, we optimize the absorbance signal for a 100-nm fibroin layer on a nanobar array on a silicon substrate. As previously mentioned, we optimize for three parameters: a) nanobar width; b) nanobar length and c) period of the nanobar arrays. In a limited number of simulations, we have explored varying the x - and y - array periods independently, but we have not seen an improvement in the optimized absorbance signal as compared to a square lattice for the range of parameters explored in this study. For all the simulations in this work, we assume nanobar thickness of 70 nm, for consistency with our previous experimental and computational studies.

Utilizing the optimization methods outlined above, we are able to obtain absorbance signal enhancement from either 6 μm - (Fig. 6(A)) or 6.6 μm -wavelength (Fig. 6(B)) peak with two separate sets of optimized geometric parameters. In Fig. 6, we plot computed A_{ref} , based on array parameters derived for the 100-nm fibroin layer optimization, for the thickness range from 5 to 200 nm. These optimized array parameters for the Si substrate are listed in first two columns of Table 1. Both the length and the period of the array need to be adjusted when re-optimizing the array for the two different wavelengths, while the width of the array changes little.

From the traces of Fig. 6, it is evident that optimization performed at a single thickness gives good results for a wide thickness range with minimal spectral distortion of the

optimized peaks. However, in generating a trace at each thickness of Fig. 6, an appropriate R_{ref} of the corresponding thickness of the transparent layer was used.

A closer inspection of a bare array reflectance spectrum, as well as reference-covered and 100-nm-fibroin-covered spectra, reveal substantial index-induced shifts that are compensated for by the optimization algorithm. (Fig. 7) It would be quite difficult to arrive at the set of optimized array parameters without a rational optimization procedure. The position of the (1,0) grating transition order (shown as a dashed vertical line in Fig. 7) occurs at a slightly lower wavelength than the peak enhancement. This location of the grating transition order allows for the lowest damping to occur near the 6- μm peak position, in confirmation of the intuition proposed in [1]. By comparison, for the array optimized by trial-and-error (See Fig. 4(A)), the position of the (1,0) grating transition is considerably further removed from the resonance. Thus, we would not expect that empirically-optimized array to perform as well in enhancing absorbance as the array whose dimensions have been optimized rigorously.

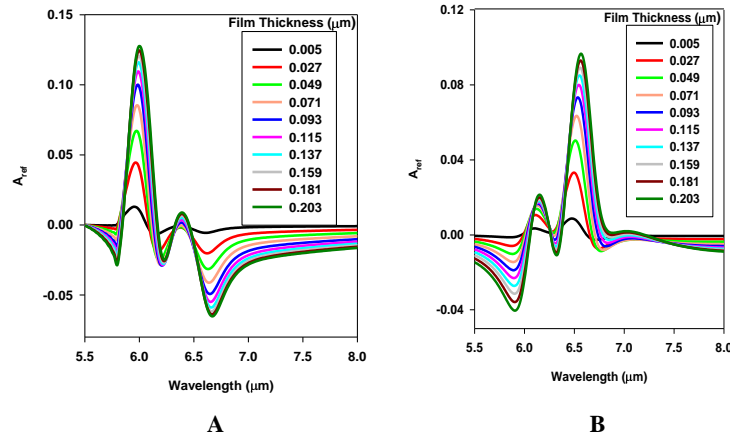


Fig. 6. Computed absorbance for fibroin-covered nanoplasmonic array whose dimensions have been optimized for A) An

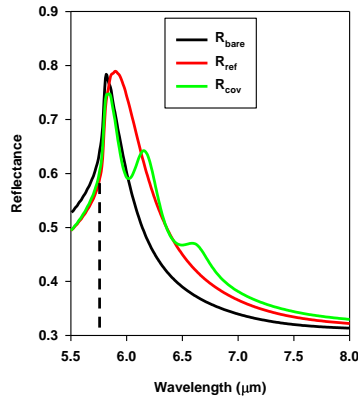


Fig. 7. Computed reflectance of a bare (R_{bare}), a 100-nm thick reference-layer covered (R_{ref}) and a 100-nm fibroin covered (R_{cov}) nanoplasmonic arrays for the optimized geometry of Fig. 6(A). The dashed vertical line indicates the position of the (1,0) diffractive edge according to Eq. (7).

Comparison of fibroin absorbance, A_{ref} , for the optimized array to the bare Au layer reveals remarkable signal enhancements of $>10^3$, especially for low-coverage regime (See Fig. 8, dashed lines), which is consistent with our previous work [1]. With increase in thickness, we observe a sublinear increase of A_{ref} (see Fig. 8, solid lines): for thicker films, the

array is less effective in enhancing absorbance due to the decrease of the near field enhancement. Corresponding to the roll-off of the integrated absorbance with thickness, we observe a decrease in signal enhancement as compared to a bare Au layer, plotted on the left hand vertical axis. For monolayer-thick films (≤ 5 nm), the average enhancement is $>10^3$, whereas for $0.2\text{-}\mu\text{m}$ thick films, the enhancement is a factor of 20, still a considerable improvement over the standard absorbance from a bare Au layer. The predicted saturation of the enhanced signal for these numerically-optimized arrays is qualitatively consistent with the previous results on experimentally-optimized arrays, although the earlier paper predicted a signal roll-off at somewhat lower thicknesses [1]. We further discuss this absorption roll-off in the context of the spatially-averaged electric field intensity decay with increasing distance from the substrate (see disc

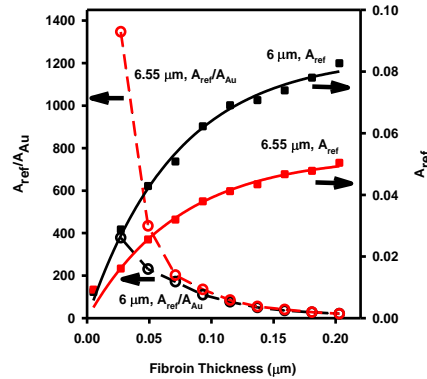


Fig. 8. Averaged absorbance over 6- and $6.55\text{-}\mu\text{m}$ peaks with increasing layer thicknesses (right vertical axis) for Si substrate. Also shown is the corresponding absorbance signal enhancement over that from a bare Au layer of Fig. 2 (left vertical axis). The solid and dashed lines are drawn to guide the eye.

CaF₂ substrate

We now repeat the optimization procedure for arrays on a CaF₂ substrate. Placing the arrays on the low index substrate has several advantages. As we show below, much higher surface electric fields are attained at resonance leading to a significantly higher absorbance signal than on Si substrate. From a practical point of view, using the low-index CaF₂ substrate reduces backside reflections and, thus, significantly suppresses interference fringes that would otherwise obscure the absorbance spectrum from a higher index Si substrate. From the refractive index ratio of the two substrates, we expect the array periodicity on CaF₂ substrate to be $2.4 \times$ larger than on Si substrate (see Eq. (7)). The nanobar length, considering n_{eff} from Eq. (6), is expected to be $\approx 2 \times$ larger on a CaF₂ substrate than on a Si substrate.

The optimized array dimensions for a 100-nm thick fibroin film on a CaF₂ substrate are summarized in Table 1, Column 3. The width of the optimized nanobars is similar for CaF₂ and Si substrates. The optimized length and period follow the scaling predictions described above for the two different substrates. Figure 9(A) shows A_{eff} vs. overlayer thickness. Comparing these results with Fig. 6(A), we observe that the peak absorbance values are substantially higher on CaF₂ substrate and that the spectra saturate for higher overlayer thickness ($>0.1\ \mu\text{m}$) as compared to the Si substrate. The difference between infrared radiation coupling into nanobars on CaF₂ vs. on Si is especially striking if we consider the % fraction of the total light absorbed into the array at resonance, assuming that all incident light is polarized along the long axis of the nanobars. For Si substrate, 10% of incident light is coupled into the array. Considering that the array geometric footprint is 5% of the substrate area (Table 1), this translates into a relative absorption cross-section of $10 \div 5 = 2$. By contrast

for CaF₂ substrate, 40% of the incident light is coupled into an array whose geometric footprint is a mere 2%, translating into a relative absorption cross-section of 20.

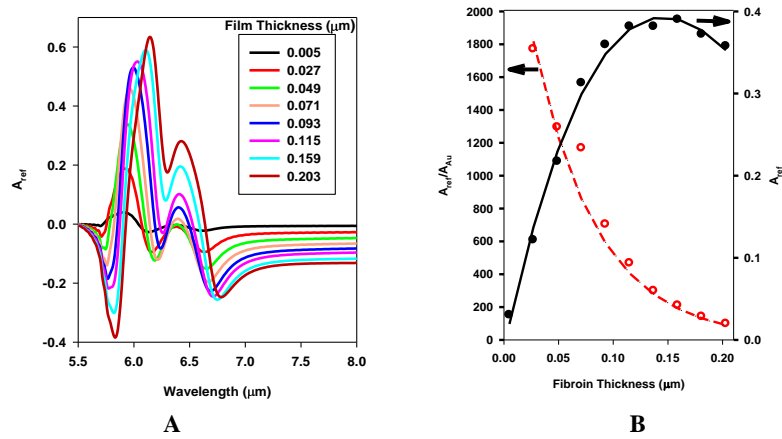


Fig. 9. Computed absorbance for an Amide I optimized fibroin-covered nanoplasmonic array on CaF₂ substrate. A) Absorbance vs. wavelength for varying overlayer thicknesses and B) Averaged absorbance vs. thickness (right vertical axis) and a corresponding absorbance signal enhancement over that from a bare Au layer (left vertical axis). The solid and dashed lines are drawn to guide the eye.

Table 1. Optimized Array Dimensions (μm)

Peak (μm)	Si Substrate		CaF ₂ substrate		
	δ^a	6.55^a	δ^a	δ^b	δ^c
Width	0.17	0.15	0.18	0.18	0.17
Length	0.85	0.96	1.71	1.85	1.85
Period	1.69	1.83	4.09	4.08	4.12

^a100-nm thick planar film; ^b6-nm thick planar film; ^c6-nm thick conformal film

Plotting averaged A_{eff} vs. thickness for the CaF₂ substrate (Fig. 9(B)) reveals much higher absorbance than that for Si substrate (cf. Figure 8) and a saturation of the absorbance with thickness above 0.1 μm . This signal saturation for the CaF₂ substrate suggests that decay of surface field with increasing distance from the metamaterial dominates the absorbance instead of the total fibroin thickness. In order to better understand the difference in thickness dependence of the absorbance signals for CaF₂ and Si substrates, we computed local electric fields for several field-monitoring cut planes, parallel to the substrate, at distances corresponding to the thickness values of Fig. 9(B). For these calculations, an infinitely thick transparent reference overlayer covers the plasmonic nanoarrays to simulate the index environment. We chose to compute the fields in a *transparent* overlayer to highlight the dependence of the local electric field on the distance from the surface, without convolving attenuation in the overlayer itself. Arrays optimized for the 6- μm peak are considered for both Si and CaF₂ substrates. For each field monitor plane (Fig. 9(B)), we compute field intensity $\langle |E|^2 \rangle$, which is averaged over the full simulation unit cell and normalized to the incident field. Through Eq. (1), $\langle |E|^2 \rangle$ is related to total absorbance.

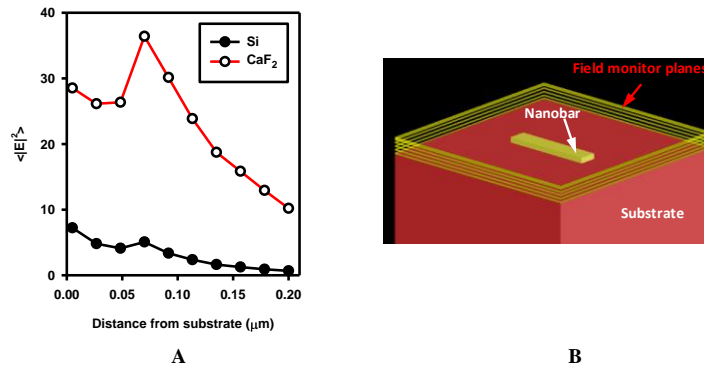


Fig. 10. (A) Area-averaged normalized field intensity, normalized to incident field, for cut planes, parallel to the substrate for nanobars on Si and CaF₂ substrate as a function of plane distance from substrate. (B) Geometry of the cut planes with respect to the substrate and the unit cell of the nanobar array.

From Fig. 10(A), we observe several marked differences for the two substrates. First of all, average field intensities are nearly 3 times higher for the CaF₂ substrate, as compared to the Si substrate. Secondly, the CaF₂ substrate has a more pronounced peak at a distance of 0.07 μm away from the substrate. This distance corresponds to the top of the nanobar. This result reveals that due to the lower CaF₂ substrate index, the maximum field location is pushed to the top of the nanobar, unlike the Si substrate, where the maximum fields are found at the Si/nanobar interface [1]. These extremely high field intensities near the top of the nanobar for the CaF₂ substrate correspond to the absorption signal saturation with overlayer thickness, calculated in Fig. 9(B). (Recall that Fig. 10 highlights field intensity distribution inside a transparent index-matching layer to emphasize the field decay due to surface enhancement in the absence of absorption; whereas Fig. 9(B) shows results of the field profile convolved with the absorption of fibroin.) We also note that the decay of the unit cell-averaged field intensity with distance is fairly gradual, by contrast with the predicted rapid peak field intensity decay away from the nanobar surface [14].

The extremely high field concentration at the top of the nanobar for a CaF₂ substrate has prompted us to re-optimize the array geometry for a thin overlayer, whose thickness is much smaller than the nanobar height. In Table 1, Columns 3 and 4, we compare optimized array dimensions for the 6- μm fibroin peak and for fibroin thicknesses of 100 nm and 6 nm respectively, both for planar coverages. The array optimized for the thin overlayer has a larger length, though the period and the width are nearly the same as for the thicker overlayer. This re-optimization procedure increases by a factor of 2 the absorbance signal from the thin planar film for array dimensions of Column 3 vs. those of Column 4 in Table 1. The results point out the sensitivity of the optimized design to the analyte layer thickness. Thus, for maximum performance, arrays for monolayer adsorption coverage or immunoassay studies should be designed differently than those for in situ tissue analysis.

We can understand the difference of the optimized geometries for thin and thick films as follows. When the nanoplasmonic array gets loaded with a progressively thicker adlayer, the optimization algorithm shifts the length of the array so as to match the loaded and the bare array reflectance signatures, maximizing A_{ref} and minimizing spectral distortions. On the other hand, the array period determines the position of the (1,0) diffraction edge. This position stays constant such that it is “optimally” related to the frequency of the protein absorption band which is independent of adlayer thickness.

Next, we compared the optimized nanoarray geometry for both planar and conformal film configurations (see Fig. 3). The results are shown in Columns 4 and 5 of Table 1, for the 6-nm thick films for planar and conformal coverages, respectively. The array optimized for

conformal coverages has the same length but a slightly larger period than that optimized for planar coverage. The absorbance of a conformal thin film on a re-optimized geometry is 1.5x that of a planar thin film on its respectively re-optimized geometry. This significant improvement in absorbance does suggest that for a properly optimized nanobar, the majority of the signal is derived from the portion of the overlayer closest to the substrate. Again, these optimization studies suggest that proper plasmonic array design should include good understanding of adsorption geometry in addition to targeting the spectral region being enhanced.

Design sensitivity studies

Having arrived at optimal array designs, as shown in Table 1, we next explore the sensitivity of such designs to dimensional tolerances that would be associated with any nanofabrication method. While the global and local optimizers utilized in this study thoroughly explore the design parameter space, the intermediate results on the way to the optimized design are not retained because of a large associated disk space overhead. Thus, the response surface for the parameter space needs to be obtained separately.

For parameter space mapping, we turn to the Design Of Experiments (DOE) method [29]. DOE is a technique that seeks to optimize the information content of simulation trials. Using fundamental statistics, one can create a list of trials that vary independent variables, such as geometric array parameters in our example, in a systematic fashion so that the absorbance response can be predicted at any intermediate setting using regression analysis. As a result, the impact of linear, non-linear and interaction terms among multiple input variables can be readily visualized. While traditionally DOE techniques are used for industrial process control, in the recent years they have been successfully applied to electromagnetic designs [30].

For our design of experiment methods, we used the commercial software package ECHIP [31]. Three design variables, width, length and period, were used to generate a full factorial three-level design with 27 simulation trials. The separate trials were analyzed with FDTD software. The results of the 27 simulations were then passed to a non-linear regression model that included linear, quadratic and interaction terms for the three variables.

We explored design sensitivity for nanobars on Si and CaF₂ substrates for the 6- μ m wavelength peak and a planar coverage of a 100 nm-thick fibroin film. The optimized values were allowed to vary by ± 50 nm from their optimum parameters for the Si substrate and by ± 100 nm for the CaF₂ substrate. This parameter range is shown in the response surface design sensitivity studies.

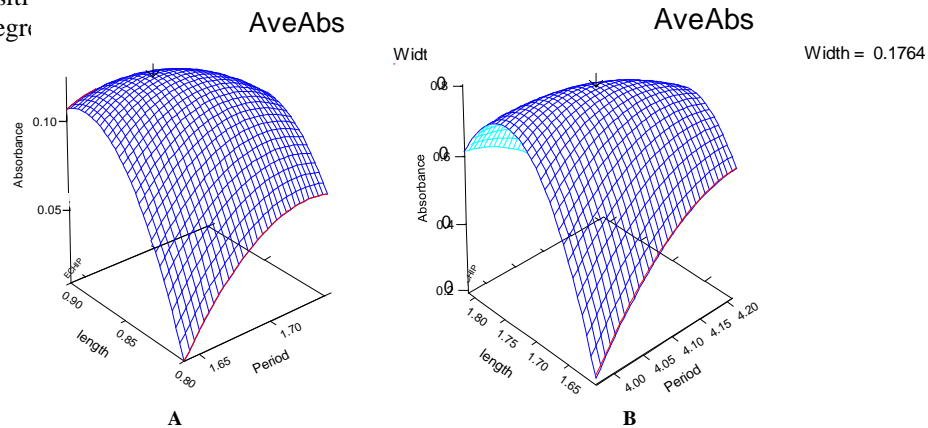


Fig. 11. Response surface of 6- μ m absorbance peak from the DOE-driven simulations for length vs. period for the nanoplasmonic arrays near their optimized conditions for the 100-nm thick fibroin film. A) Si substrate for the conditions of Table 1, Column 1 and B) CaF₂ substrate for the conditions of Table 1, Column 3. The off-axis width variables are set to the optimized values.

The results of the analysis (Fig. 11) show the 3D surface plots of the absorbance response, spectrally averaged over the 6- μm peak, for the length vs. period for the Si substrate (Fig. 11(A)) and CaF_2 substrate (Fig. 11(B)). For both figures, the off-axis variable is at the optimum design value. We note that absorbance is less sensitive to dimensional change near the optimum response, whereas the contour surface becomes steeper away from the optimum spot. We also see a clear local maximum in Fig. 11 for a particular value of nanobar spacing, consistent with our previous experimental data [1]. For the range of parameters explored, very little absorbance change with nanobar width was observed. If 20% response decrease from the maximum value is acceptable, then the length can depart by ± 25 nm from the design, and both the period and the width can change by more than ± 50 nm from the design value on either Si or CaF_2 substrates. Such dimensional tolerances are certainly achievable over large areas utilizing modern nanofabrication techniques, such as mask-based photolithography or maskless interference lithography.

Conclusion

We have provided a framework for efficient numerical optimization of plasmonic substrates for SEIRA enhancement. Importantly, for the first time, our framework explicitly compensates for the perturbative effects of the analyte, with respect to spectral distortions, thickness variation and adsorption geometry. Our optimization method is sufficiently general that it can be extended to various nanostructure geometries, analytes and sensing configurations.

We have demonstrated our method for IR absorbance enhancement of silk protein analyte with a diffractively-coupled plasmonic nanobar array for normal incidence. We have considered the effect of substrate index variation, the effect of film thickness and coating geometry. We find that three-order of magnitude absorbance enhancement is possible as compared to an unstructured Au layer; however, the proper array optimization should be tailored to the film thickness range expected, i.e., monolayer absorbance studies vs. thicker tissue analysis.

For our model silk fibroin system, we have correlated surface-enhanced absorbance fall-off vs. distance from substrate with experimental studies. Particularly, we find that average enhancement can extend >100 nm from the surface and that it is dependent on the substrate index.

Finally, we performed sensitivity analysis due to fabrication imperfections, utilizing DOE technique. We believe that $< 20\%$ of the deviation from the optimized absorbance response is readily achievable for our diffractively-coupled arrays over large areas.

Acknowledgments

This work is sponsored by the Assistant Secretary of Defense for Research & Engineering under Air Force Contract #FA8721-05-C-0002. Opinions, interpretations, conclusions and recommendations are those of the author and are not necessarily endorsed by the United States Government. The Boston University portion of this work was supported by MIT Lincoln Laboratory, an NIH Grant 1 R21 EB013381-01 and NSF award number 0821450 and NSF I/UCRC grant number NSF IIP-1068070.